

**IDENTIFYING ELECTRONIC PROPERTIES RELEVANT TO
IMPROVING THE PERFORMANCE AND STABILITY
OF AMORPHOUS SILICON BASED
PHOTOVOLTAIC CELLS**

Annual Subcontract Report 27 November 2001- 26 November 2002

J. David Cohen
Department of Physics and Materials Science Institute
University of Oregon, Eugene, Oregon

**Prepared for the National Renewable Energy Laboratory
under Subcontract No. ADJ-2-30630-17**

NREL Technical Monitor: B. von Roedern

PREFACE

This Annual Technical Progress Report covers the work performed at the University of Oregon for the period 27 November 2001- 26 November 2002 under NREL Subcontract Number ADJ-2-30630-17. The following personnel participated in this research program:

NAME	TITLE	WORK PERFORMED
J. David Cohen	Principal Investigator	Program Manager
Jennifer Heath	Research Assistant	Properties of BP Solar a-Si:H samples deposited at high rates.
Suman Iyer	Visiting Scientist	Properties of BP Solar a-Si:H samples deposited at high rates.
James Gutierrez	Research Assistant	Properties of NREL a-Si,Ge:H samples and United Solar mixed phase materials; some work on high deposition rate BP Solar samples

TABLE OF CONTENTS

	Page
LIST OF ILLUSTRATIONS	iv
LIST OF TABLES	v
EXECUTIVE SUMMARY	vi
 1.0 INTRODUCTION.....	 1
 2.0 SAMPLES	
2.1 HIGH GROWTH RATE SAMPLES PRODUCED AT BP SOLAR.....	1
2.2 HIGH GERMANIUM FRACTION a-Si ₁ Ge ₁ :H HWCVD ALLOYS.....	2
2.3 AMORPHOUS SILICON AT THE EDGE OF MICROCRYSTALLINITY	3
 3.0 EXPERIMENTAL CHARACTERIZATION METHODS	
3.1 ADMITTANCE SPECTROSCOPY	4
3.2 DRIVE-LEVEL CAPACITANCE PROFILING.....	4
3.3 TRANSIENT CAPACITANCE SPECTROSCOPY	5
3.4 TRANSIENT PHOTOCAPACITANCE AND PHOTOCURRENT.....	6
 4.0 ELECTRONIC PROPERTIES OF HIGH-GROWTH RATE a-Si:H MATERIAL	
4.1 REVIEW OF PREVIOUSLY REPORTED RESULTS	7
4.2 CORRELATION BETWEEN DEFECT DENSITIES AND DEVICE PERFORMANCE	9
4.3 STUDIES ON NEW SERIES OF BP SOLAR HIGH GROWTH RATE SAMPLES.....	12
 5.0 HOT-WIRE a-Si₁Ge₁:H MATERIAL AT HIGH GERMANIUM FRACTION .	 17
 6.0 UNITED SOLAR AMORPHOUS SILICON NEAR PHASE BOUNDARY	 19
 7.0 SUMMARY AND CONCLUSIONS.....	 20
 8.0 SUBCONTRACT SUPPORTED PUBLICATIONS	 22
 9.0 REFERENCES.....	 22

LIST OF ILLUSTRATIONS

	Page
FIG. 1. Schematic of the appearance of United Solar mixed phase samples	3
FIG. 2. Schematic diagram indicating the basic sequence of events in semiconducting junction transient measurements.....	7
FIG. 3(a) Monotonic loss of device efficiency with increasing growth rate 3(b) Defect densities obtained from DLCP measurements vs. growth rate.....	8
FIG. 4(a) Photocapacitance spectra for the BP Solar 1.5Å/s growth rate sample 4(b) Example of how photocapacitance spectra are fit.....	9
FIG. 5. The Urbach energies deduced from the photocapacitance spectra correlate fairly strongly with the sample growth rates.....	9
FIG. 6. Magnitude of deep defect band deduced from TPC spectra vs. matched device fill factor	10
FIG. 7. Drive-level capacitance profiles for 3Å/s BP Solar sample in the dark annealed state	13
FIG. 8. Deep defect densities vs. growth rate for BP Solar films for both States A and B...	14
FIG. 9(a) Photocapacitance spectra for BP Solar sample L2127 9(b) CPM spectra obtained at NREL for the same sample.....	14
FIG. 10. Urbach energies determined from TPC spectra vs. film growth rate.....	15
FIG. 11. Photocapacitance spectra for two BP Solar films in State A	17
FIG. 12. Drive-level capacitance profiles for 63at.% Ge fraction a-Si _{0.37} Ge _{0.63} :H film deposited by HWCVD at NREL	18
FIG. 13. Photocapacitance spectrum for the same a-Si _{0.37} Ge _{0.63} :H sample.....	18
FIG. 14 Drive-level profiles for a region near the center of mixed phase United Solar film L13698	20

LIST OF TABLES

TABLE I.	HWCVD a-Si,Ge:H samples provided by NREL.....	3
TABLE II.	Results on BP Solar films in the annealed state and after light soaking listed in order of increasing growth rate	11
TABLE III.	Summary of cell parameters in State A for matched BP Solar devices.....	13
TABLE IV.	Comparison of TPC determined Urbach energies with growth rate, hydrogen content, void fraction, and CPM determined Urbach energies.....	16

EXECUTIVE SUMMARY

During this first phase of our NREL Subcontract ADJ-2-30630-17 we have focused primarily upon studies to try to identify the fundamental reasons that higher growth rate a-Si:H materials lead to devices with generally lower performance. These studies utilized series of samples produced by Gautam Ganguly at BP Solar. Previously, our measurements had revealed that the deep defect density determined by drive-level capacitance profiling (DLCP) did not change as the growth rate was varied; however, the Urbach energies deduced by transient photocapacitance (TPC) sub-band-gap spectroscopy *were* correlated with growth rate and hence also the device performance. During the past year we have found that the magnitudes of the deep defect revealed in the TPC spectra correlate quite well with the device fill factors, even though the DLCP determined defect densities do not. Thus we propose that the capture cross section of the deep defects are enhanced at the higher growth rates even though their actual density do not vary substantially.

We also report results from a second study in collaboration with BP Solar. These employed a new series of samples deposited by Gautam Ganguly, and our own study was one part of a five-way collaboration with NREL, Colorado School of Mines, University of North Carolina, and BP Solar. Results for this new series of samples agreed with the previous set in that the DLCP determined defect densities appeared to be largely uncorrelated with device performance, while the Urbach energies were strongly correlated. The other studies of the collaboration revealed that the void fraction and the hydrogen content were also quite strongly correlated with growth rate. Once again, the cell performance exhibited a systematic decline in performance with increasing growth rate.

During this past year we also examined a couple NREL HWCVD a-Si_xGe_{1-x}:H alloy samples with Ge fractions exceeding 60at.%. These samples had somewhat poor electronic properties: non-uniform and somewhat high defect densities and very broad Urbach energies. These new results are in agreement with results from our previous studies of HWCVD a-Si_xGe_{1-x}:H samples with higher Ge content. Finally, we began a collaborative study with United Solar to examine material at or beyond the phase transition boundary to microcrystallinity. Some preliminary results are reported.

1.0 INTRODUCTION

The work carried out in Phase I under NREL Subcontract ADJ-2-30630-17 has concentrated on three general types of studies. First, we have continued our examination of the electronic properties of high growth rate, a-Si:H samples produced at BP Solar in collaboration with Gautam Ganguly using the DC glow growth process. In addition to continued work on the previous series of samples, we have characterized a new set of 4 samples as part of a five-way collaboration with other NREL amorphous silicon Team members. This collaborative study has resulted in a much more detailed characterization of the structural properties of these high growth rate samples to compare with their deduced electronic properties.

Second, we have begun to characterize a series of higher Ge fraction a-Si_xGe_{1-x}:H alloy samples deposited by the hot-wire technique by Brent Nelson at NREL. The samples with more than 50at.% Ge indicated very broad Urbach tails as determined by our transient photocapacitance sub-band-gap spectroscopy, consistent with the higher Ge fraction a-Si_xGe_{1-x}:H samples deposited by HWCVD we had measured previously.

Finally, we have begun a study to examine samples across the phase boundary between amorphous and microcrystalline silicon. These measurements utilize samples produced at United Solar Systems in which a single deposition contains regions spanning material that is predominantly amorphous in nature to material that is dominated by its microcrystalline component.

In the Sections that follow, we first describe the samples studied and then briefly review the experimental techniques employed. In Section 4 we discuss our results concerning the high growth rate samples deposited at BP Solar. In Section 5 we present very preliminary results on the a-Si_xGe_{1-x}:H HWCVD samples obtained from NREL. In Section 6 we discuss our preliminary results a series of United Solar samples which are partially nanocrystalline. Finally, in Section 7 we will summarize our findings and try to draw some general conclusions.

2.0 SAMPLES

2.1 HIGH GROWTH RATE SAMPLES PRODUCED AT BP SOLAR

Previously Gautam Ganguly at BP Solar had sent us a series of of nine samples to examine the properties of these DC glow discharge a-Si:H films as the growth rate varied due to different levels of hydrogen dilution and glow discharge power. For this set of samples the growth rate varied between 0.65Å/s and 6.0Å/s. While many of the results on this series of samples were

given previously [1], additional and potentially important new results on this series of samples were obtained during the past Subcontract year.

Indeed, the new results on these samples helped motivate a new set of studies involving several different research groups within the amorphous silicon Team. In addition to BP Solar and the University of Oregon, this collaboration included the University of North Carolina (Daxing Han), the Colorado School of Mines (Don Williamson), and NREL (Brent Nelson). These studies employed a new series of samples from BP Solar for which the growth rates were 1Å/s, 3Å/s, 5Å/s and 10Å/s.

Films for our measurements were deposited onto smooth TCO coated glass with thicknesses ranging between 1.5 to 1.8 microns as determined by Dektak profiling. Matched p-i-n devices were fabricated in a glass/SnO₂/p/i/n/ZnO/Al structure (specular SnO₂) using the identical series of growth conditions. For the devices the i-layer thickness was kept close to 0.25µm. Simultaneous light-soaking treatments of the films and devices were carried out at the University of Oregon.

Films were also simultaneously deposited onto textured TCO coated glass for photoluminescence measurements carried out by Daxing Han. She also measured electroluminescence and IR absorption. Films were also co-deposited onto Al-foil substrates so that Don Williamson could carry out SAXS measurements. Finally, CPM measurements were carried out by Brent Nelson and his collaborators at NREL, using films co-deposited onto bare glass substrates.

All of the films and devices were characterized in their as-grown state (State A) and a subset were characterized in a light-degraded state (State B). The light-degraded state was obtained by illuminating the films and devices for 100 hours using the same red-filtered ELH light source at an intensity of 100 mW/cm². In degrading the films we were careful to compensate for the partial transparency of the Pd contacts.

2.2 HIGH GERMANIUM a-Si_{1-x}Ge_x:H HWCVD ALLOYS

During the past year we began to characterize a series of a-Si_{1-x}Ge_x:H alloys deposited by the hot-wire CVD method at NREL. This collaboration was initiated by Brent Nelson who sent us four a-Si_{1-x}Ge_x:H films deposited on c-Si, quartz, and glass substrates. Table I lists the substrate temperature, growth rates, and the Ge and hydrogen fractions determined by subsequent SIMS analysis for these samples. We attempted to characterize the films deposited onto the c-Si substrates using our junction capacitance methods (DLCP and TPC spectroscopy). A semi-

TABLE I. HWCVD a-Si,Ge:H samples provided by NREL, indicating the substrate temperature and deposition rate. SIMS analysis was used to determine the germanium and hydrogen content. For the values denoted with an *, the SIMS analysis was not carried out on the actual film of the denoted run, but on a film deposited under nominally the same conditions.

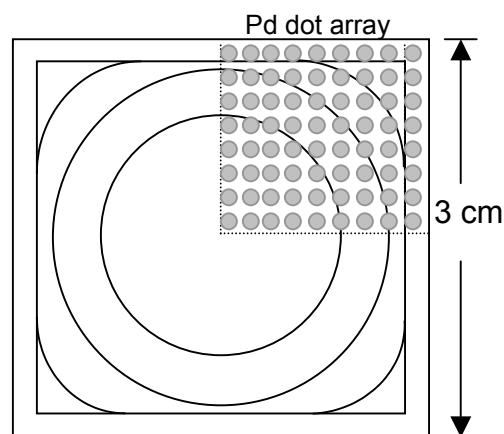
Run #	Substrate Temperature (°C)		Ave. Dep. Rate (Å/s)	SIMS Analysis (at.%)	
	Begin	End		Germanium	Hydrogen
L748	250	305	8.44	38	9
L750	250	300	7.33	38*	9*
L752	125	190	2.47	63*	18*
L753	125	268	2.76	63*	18*

transparent Pd contact was deposited onto the top surface of each sample. Unfortunately we found that good junction capacitance characteristics could only be achieved for the L753 sample.

2.3 AMORPHOUS SILICON AT THE EDGE OF MICROCRYSTALLINITY

During this year we attempted to examine the metastable properties of a-Si:H films deposited near and just beyond the edge of the microcrystalline phase transition. We obtained two sample arrays from United Solar, each of which was produced in a single deposition, but which ranged from nearly purely amorphous to very microcrystalline over a 1-2 cm distance. Such samples can be produced in their glow discharge reaction using a level of hydrogen dilution very close to the value of the amorphous to microcrystalline phase boundary. This meant that the small rf power density variation across the diameter of the 2" x 2" substrate resulted in variations of the microcrystalline fraction in a very significant manner. The sample structures were SS/n/i with the i layers roughly 2 microns thick. A schematic diagram of the different regions the occur in the two samples we received in shown in Fig. 1 below.

FIG. 1. Schematic of the appearance of United Solar samples L13690 and L13698. These films were deposited very close to the amorphous/microcrystalline phase boundary. The innermost circle was the most amorphous in appearance, the next 2 concentric circles appeared much grayer due to their increasing microcrystalline fraction. We deposited Pd 1mm diameter dots across one quadrant of each sample as indicated to attempt to explore the variation in electronic properties as the microcrystalline fraction was increased.



These films are similar to the array of cells researchers at United Solar employed in their recently reported study in which an unusual variation in open circuit voltage with light-induced degradation was observed depending on the microcrystalline fraction in that part of the sample.[2] Thus, we are hoping to gain some insight into the changes in the electronic properties of these films (in going from more amorphous to more microcrystalline) that might help us understand the unusual changes in V_{OC} with light soaking that were disclosed in the United Solar study.

3.0 EXPERIMENTAL CHARACTERIZATION METHODS

The measurements employed in our studies rely on a set of experimental techniques which have all been described previously in some detail. They consist of (1) admittance spectroscopy as a function of temperature and frequency, (2) drive-level capacitance profiling, (3) transient capacitance spectroscopy, and (4) transient photocapacitance taken together with transient junction photocurrent spectroscopy. Here we will describe each method only very briefly and review what kind of information is obtained from each type of measurement.

3.1 ADMITTANCE SPECTROSCOPY

Our Schottky diode samples contain a depletion region which is characterized as a function of temperature and frequency before we undertake the more sophisticated capacitance based measurements described in Sections 3.2 to 3.4 below. Such measurements provide us with an estimate of our film thickness (the temperature independent region at low T is simply related to the geometric thickness, d , by the formula $C = \epsilon A/d$), and an Arrhenius plot of the frequency of the lowest temperature capacitance step (or conductance peak) *vs.* $1/T$ provides us with the activation energy of the ac conductivity, E_{σ} , which we identify with the Fermi energy position: $E_{\sigma} = E_C - E_F$. [3] These admittance measurements also give us an indication of the quality of our Schottky barriers which allow us to pre-screen our samples for further study.

3.2 DRIVE-LEVEL CAPACITANCE PROFILING

The drive-level capacitance profiling method has been described in detail in many publications [4,5]. It is similar to other kinds of capacitance profiling in that it provides us with a density *vs.* distance profile; however, this particular method was developed specifically to address the difficulties encountered in interpreting capacitance measurements in amorphous semiconductors. In this method we monitor the junction capacitance both as a function of DC

bias, V_B , and as a function of the amplitude of the alternating exciting voltage, δV . One finds that to lowest order this dependence obeys an equation of the form:

$$C(V_B, \delta V) = C_0(V_B) + C_1(V_B) \delta V + \dots$$

and that the ratio

$$N_{DL} \equiv \frac{C_0^3}{2q_e \epsilon A^2 C_1} \quad (1)$$

is directly related to an integral over the density of mobility gap defect states:

$$N_{DL} = \int_{E_c - E_e}^{E_F^0} g(E) dE \quad (2)$$

Here E_F^0 is the bulk Fermi level position in the sample and E_e depends on the frequency and temperature of measurement:

$$E_e(\omega, T) = k_B T \log(v/\omega) \quad (3)$$

Thus, by altering the measurement temperature (or frequency) we obtain information about the energy distribution of the defects and, by altering the applied DC bias, we can vary the spatial region at which we detect the defects in the sample. That is, we can spatially profile the defects as a function of the position from the barrier interface.

In our current studies we typically measured 10 or 100Hz profiles for a series of temperatures between 320K to 360K. These data usually indicated a clear upper limit for N_{DL} which, we have shown [6], is equal to roughly one half the total defect density in these samples. This thus provides us with a quantitative measurement of the deep defect levels. In addition, because of the profiling information also obtained, we are able to assess the spatial uniformity of the electronic properties in these samples.

3.3 TRANSIENT CAPACITANCE SPECTROSCOPY

The general method of junction transient measurements on amorphous semiconductors has been discussed in detail in several earlier publications.[3,7,8] The basic physics of all such measurements is as shown in Fig. 2. We illustrate the situation for a semiconductor with one discrete deep gap states within the space charge region of a Schottky barrier which is subjected to a voltage "filling pulse". This pulse causes a non-equilibrium (filled) occupation of gap state to be established. As time progresses, the initial steady-state population is recovered through the

excitation of trapped electrons to the conduction band where they can then move out of the depletion region under the influence of the electric field. In the dark this process proceeds entirely by the thermal excitation of trapped carriers. However, this process can be enhanced through optical excitation and this is the basis of the photocapacitance and junction photocurrent techniques described in Section 3.4 below.

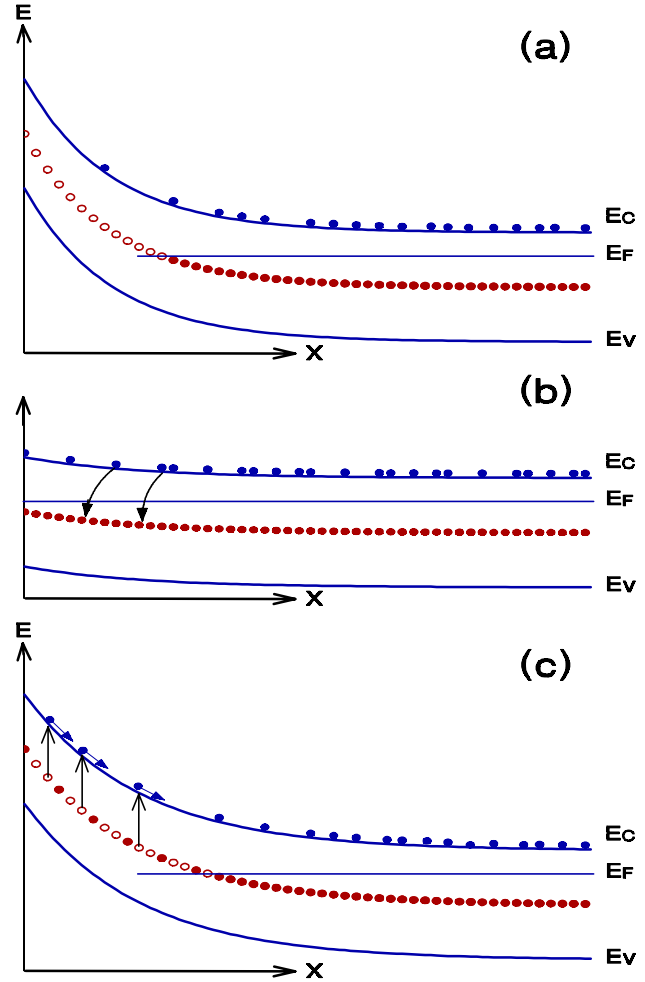
The re-equilibration can be observed by the redistribution of trapped carriers, either as a change in the *junction capacitance* (which occurs because the depletion region will contract as negative charge is lost and the positive charge density increases) or by monitoring the *current* which results from the motion of this charge. However, the observation of capacitance transients has one significant difference compared to current transient measurements: The dominant type of emitted carrier (electron or hole) can be identified by the *sign* of the observed change in capacitance.

3.4 TRANSIENT PHOTOCAPACITANCE AND PHOTOCURRENT

The methods of junction transient photocapacitance and photocurrent have been discussed by us in great detail over the years in the literature [9,10,11] and also in previous NREL reports. They represent types of sub-band-gap optical spectroscopy and provide spectra quite similar in appearance to PDS derived sub-band-gap optical absorption spectra or to CPM spectra. Instead of detecting absorbed energy, however, our photocapacitance and photocurrent transient methods detect the optically induced change in defect charge within the depletion region. However, unlike the CPM method, both of our junction based techniques are not greatly influenced by the free carrier mobilities since, once an electron (or hole) is optically excited into the conduction (valence) band it will either totally escape the depletion region on the slow timescale of our measurement (0.1 to 1s) or be retrapped into a deep state and not escape. In most cases we assume that almost all of the optically excited majority carriers (electrons) *do* escape but, in general, only a fraction of the minority carriers (holes).

Because the photocapacitance and photocurrent measurements have different sensitivities to the loss of electrons *vs.* holes from the depletion region, a detailed comparison of the two kinds of spectra can be used to disclose the escape length of the holes.[9,12] This allows us to estimate the hole $\mu\tau$ products for these samples. In these experiments the parameter τ is identified as a deep trapping time, *not* a recombination time. We are also able to distinguish whether optical excitation of defect states comes about because of the excitation of trapped electrons to the conduction band or because of the excitation of valence band electrons into an empty mobility gap state. This ability to distinguish electron from hole processes is unique among all the various types of sub-band-gap optical spectroscopies.

FIG. 2. Schematic diagram indicating the basic sequence of events in semiconducting junction transient measurements:
(a) Junction under reverse bias in quasi-equilibrium showing the electronic occupation of gap states (solid circles) plus empty gap states above E_F in deep depletion (open circles).
(b) During voltage "filling pulse" gap states capture electrons from the conduction band.
(c) Reverse bias is restored and occupied gap states above E_F are slowly released to the conduction band due to thermal or optical excitation processes.



4.0 ELECTRONIC PROPERTIES OF HIGH-GROWTH RATE a-Si:H MATERIAL

4.1 REVIEW OF PREVIOUSLY REPORTED RESULTS

In a collaborative study with Gautam Ganguly at BP Solar, we have been examining DC glow discharge a-Si:H samples whose deposition rate was varied by changing the hydrogen dilution or discharge power levels. The first series of studies examined six samples whose growth rates varied between $0.65\text{\AA}/\text{s}$ to $6\text{\AA}/\text{s}$. Matching solar cell devices for these films were characterized at BP Solar. Both the films and devices were characterized in their as-grown states (State A) and a degraded state (State B) using the identical light source (red-filtered ELH light at an intensity of $100\text{mW}/\text{cm}^2$ for 100 hours). In degrading we were careful to compensate for the partial transparency of the Pd contacts deposited on the films for our junction capacitance based measurements.

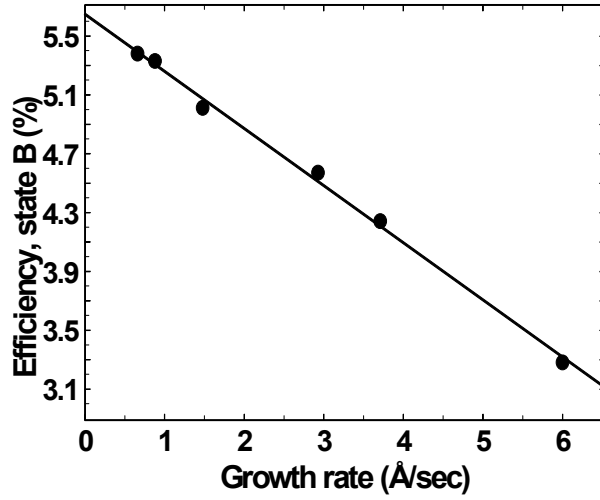


FIG. 3(a). A monotonic loss of device efficiency in the degraded state is observed with increasing growth rate.

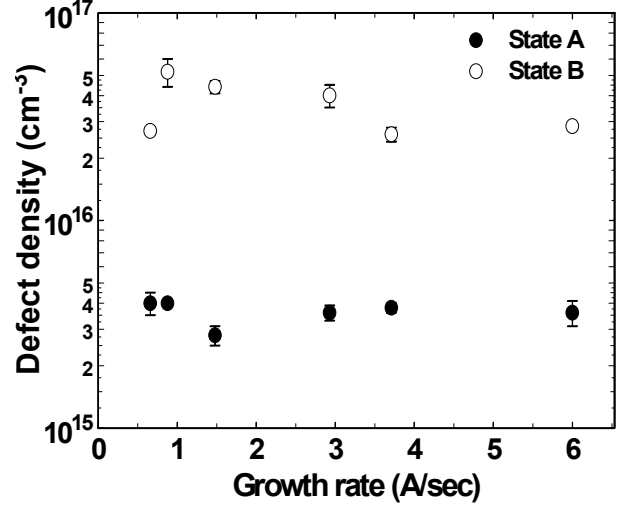


FIG. 3(b). Defect densities obtained from DLCP measurements are roughly independent of growth rate for both state A and state B (light degraded).

As we reported previously [1], there was a clear inverse relation between the device performance and the growth rate for this series of samples [Fig. 3(a)]. Also as reported previously, and shown in Fig. 3(b), there was essentially *no correlation* between the defect densities in these samples for either state A or state B, and the growth rate. The fact that the magnitude of the deep defect density determined by DLCP was nearly constant, independent of growth rate in both state A and state B, was quite a surprising result given the clear monotonic variation in device performance. It prompted our further characterization of these films using transient photocapacitance spectroscopy (TPC). The TPC technique essentially yields an optical absorption spectrum with a very high sensitivity. A pair of typical TPC spectrum for one film in states A and B is shown in Fig. 4(a). Such spectra are well fit using a combination of a gaussian band of deep defects plus an exponential band of tail states. An example of such a fit to one photocapacitance spectrum is shown in Fig. 4(b).

As also reported last year, the Urbach energies determined from these spectra *did* correlate reasonably well with growth rate such that higher growth rates exhibited broader band tails. The dependence of Urbach energy with growth rate is shown in Fig. 5. The broadening of the bandtail is not too surprising given that void densities are known to increase substantially for glow discharge samples as the deposition rate increases. On the other hand, it then seemed surprising to us that the deep defect densities did *not* seem to increase with the increasing value of the Urbach energy given the predicted relationship between the two from defect equilibration models.

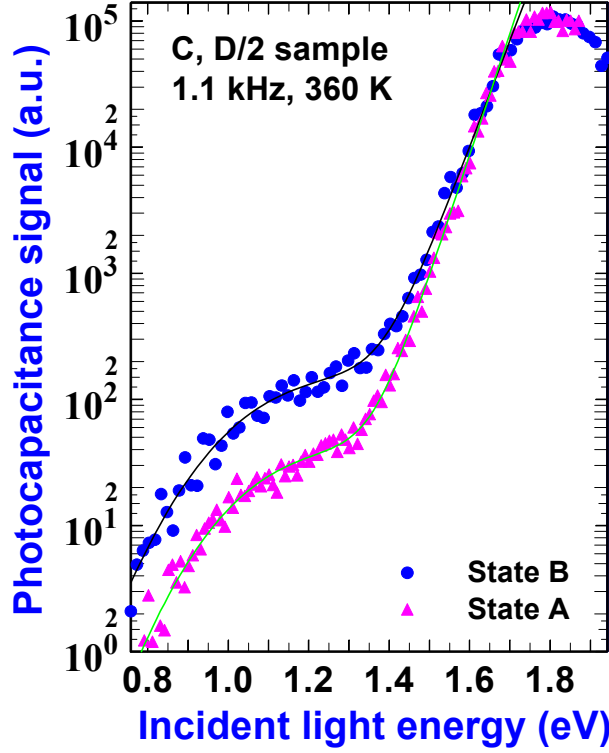


FIG. 4(a). Photocapacitance spectra for a 1.5 Å/s growth rate sample in both the annealed state and the light-degraded state.

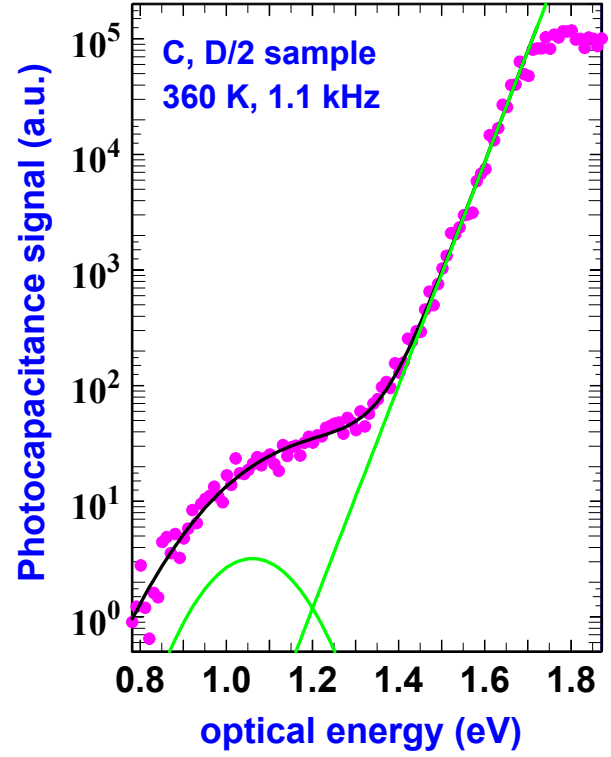
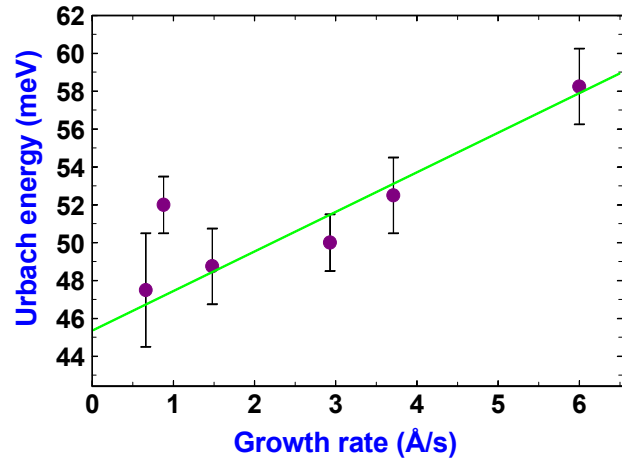


FIG. 4(b). Example of how spectra are fit with an exponential bandtail plus a Gaussian shaped defect band. We deduce relative deep defect magnitudes for different samples by aligning these spectra at the optical gap (E04) energy.

FIG. 5. The Urbach energies deduced from the photocapacitance spectra correlate fairly strongly with the sample growth rates.



4.2 CORRELATION BETWEEN DEFECT DENSITIES AND DEVICE PERFORMANCE

During the past year we decided to examine more closely whether there might be a correlation between the magnitudes of defect density determined via our sub-band-gap spectra and device performance. Indeed, while the deep defect magnitudes determined from DLCP

remain nearly constant across this series of samples (Fig. 3b), the defect band revealed in the sub-band-gap photocapacitance spectra *does* seem to exhibit a fairly strong dependence on growth rate. To compare the defect band signals for different samples we have scaled the TPC results to have an identical magnitude at the optical (E_{04}) gap. This then allows us to estimate relative values for the deep defect band magnitudes contained in the gaussian band. [see Fig. 4(b)]

It is important to note that, in several previous studies of a-Si:H using DLCP together with TPC, it has been demonstrated that both methods give essentially identical results for both the magnitude and energy distribution of the deep defect band (except that the optical energies are perhaps 80meV larger compared to the corresponding thermal activation energy determined by DLCP).[6] However, the TPC derived defect densities for these samples, in contrast to the DLCP results, actually do seem to correlate quite well with device performance, as is illustrated in Fig. 6(a). The TPC defect densities for state A and state B appear quite closely linked as well, as shown in Fig. 6(b). A summary of the Urbach energies and deep defect densities deduced by the DLCP measurements in both states A and B, along with the relative defect magnitudes deduced by the TPC measurements are summarized in Table II.

This series of companion thin film and device samples thus appears to have provided a valuable testing ground for previously proposed relationships between E_U , deep defect density, and device performance. Indeed, the strong correlation between E_U , the state B defect density, and the device performance observed in this study has not been previously reported. We've noted that defect densities and device performance are most closely correlated in state B. This may be expected since materials properties are likely to dominate in the highly degraded state while, in state A, characteristics such as the quality of the junctions and interfaces may be more

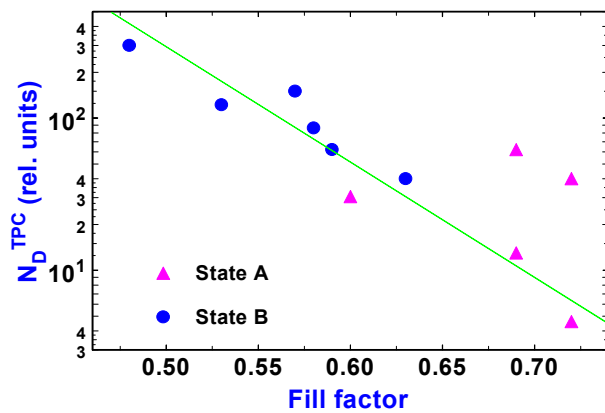


FIG. 6(a). Magnitude of deep defect band deduced from TPC spectra vs. matched device fill factor. Correlation is quite strong, particularly in the light degraded state.

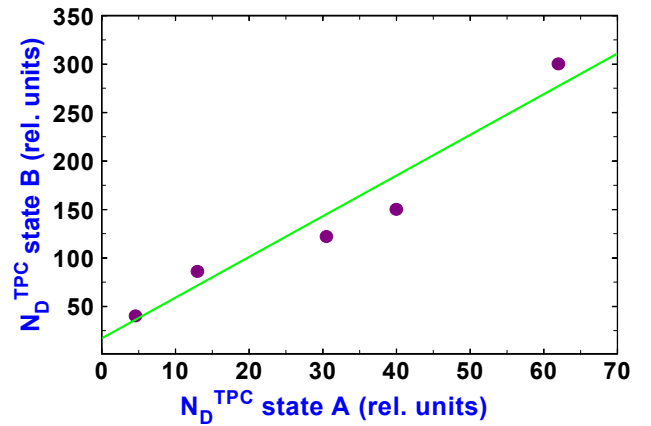


FIG. 6(b). Defect band magnitudes determined from TPC spectra in states A and B are related by nearly a constant factor.

Table II. Film results for samples in the annealed state (State A) and after light soaking (State B) are listed in order of increasing growth rate. These include defect densities obtained from drive level capacitance profiling (N_D^{DLCP}) and from transient photocapacitance spectroscopy (N_D^{TPC}).

Growth Rate (Å/s)	Relative Discharge Power	Relative Hydrogen Dilution	E_U (meV)	State A		State B	
				N_D^{TPC} (a.u.)	N_D^{DLCP} (cm ⁻³)	N_D^{TPC} (a.u.)	N_D^{DLCP} (cm ⁻³)
0.66	C	2D	48	4.6	4.0×10^{15}	40	2.7×10^{16}
0.88	C	D	52	--	5.4×10^{15}	62	6.8×10^{16}
1.5	C	D/2	49	40	2.8×10^{15}	150	4.4×10^{16}
2.9	5C	D	50	13	3.6×10^{15}	86	4.0×10^{16}
3.7	5C	2D	53	31	3.8×10^{15}	120	2.6×10^{16}
6.0	5C	D/2	58	62	3.6×10^{15}	300	2.5×10^{16}

important limiting factors. On the other hand, two of the samples in state A have very good device performance, but exhibit TPC determined defect densities nearly as large as some state B samples [the points lying farthest off the line in Fig. 6(a)]. While we are currently unable to offer an explanation for this, it is interesting to note that these are the two samples deposited with the lowest degree of hydrogen dilution for this series of samples.

Thus a very puzzling aspect of the data presented above is the large difference between the defect densities determined by the DLCP method, which do not appear to be correlated to the device performance, and those determined by the TPC spectra, which definitely are. Also, we have noted that previous studies, which applied both types of measurements to the same samples, generally indicated good agreement between the defect densities determined by the two methods[6]. In this case there is a marked difference; indeed, the DLCP defect densities hardly vary with growth rate at all! A lack of correlation between deduced deep defect densities in films and performance of matched devices has also been noted in several other studies.[13,14,15] However, in nearly all of those cases the deep defect densities were estimated using the constant photocurrent method (CPM).

One appealing explanation is that the *intrinsic properties* of the deep defects are changing with growth rate in a manner that is reflected in TPC but not the DLCP or CPM measurements. For some time researchers (particularly at Penn State University) have been suggesting an important role for charged metastable defects.[16] This was to account for the observed magnitude of device degradation compared to the modest densities of metastable defects disclosed by CPM measurements. Charged defects, with their presumably much larger carrier

capture cross sections, would lead to higher carrier recombination rates and poorer device performance.

Such an explanation might be invoked for our results as well, particularly when we note that deep defects with larger optical cross sections would appear larger in magnitude for TPC spectra, *but not for CPM*. This is because any increase in cross section, if it affected both emission and capture, would cancel out of CPM (since it is a steady-state method), but definitely enhance the optically induced carrier emission rate detected by TPC. Thus, a significant increase in the fraction of charged versus neutral deep defects with growth rate could account for our results. An alternative hypothesis to an increased density of charged defects might be that the deep defects in higher growth rate material have larger carrier cross sections because they reside near voids or in more strained environments. Indeed, it is well known that increased growth rate leads to a higher microvoid density in glow discharge samples.

4.3 STUDIES ON NEW SERIES OF BP SOLAR HIGH GROWTH RATE SAMPLES

Motivated in part by the results reported in Section 4.2, Gautam Ganguly organized a larger scale collaboration to investigate the detailed change in properties of the BP Solar DC glow discharge samples as the growth rate was increased. A new series of samples was produced using four different growth rates ranging from $1\text{\AA}/\text{s}$ to $10\text{\AA}/\text{s}$ (see Section 2.1). The series of studies on these samples involved a five way collaboration among BP Solar, the University of Oregon, University of North Carolina (Daxing Han), School of Mines (Don Williamson), and NREL (Brent Nelson)

The electronic properties of the films deposited onto the TCO coated glass were characterized by junction capacitance measurements at the University of Oregon, and included measurements the deep defect densities, electrical conductivities, and sub-band-gap photocapacitance spectra. The textured TCO coated glass films were sent to Daxing Han for photoluminescence, electroluminescence, and IR absorption. Films were also deposited onto bare quartz substrates and are intended for future ESR measurements to determine neutral dangling bond densities. Aluminum foil substrate films were characterized by SAXS measurements by Don Williamson. Finally, a set of films were deposited onto bare glass substrates and were prepared for CPM measurements by depositing Cr coplanar contacts. Those CPM measurements were carried out by Brent Nelson and his collaborators at NREL.

Both the films and devices were characterized in their as-grown state (State A) and a subset were characterized in a light-degraded state (State B). The light-degraded state was obtained by illuminating the films and devices for 100 hours using the same red-filtered ELH light source at

TABLE III. Summary of cell parameters in State A for matched BP Solar devices.

Sample	Growth Rate (Å/second)	V_{OC} (volts)	J_{SC} (mA/cm ²)	FF	Efficiency (%)
L2127	1	0.89	11.26	0.71	7.16
L2129	3	0.90	10.72	0.72	6.96
L2136	5	0.89	10.70	0.68	6.49
L2137	10	0.90	9.41	0.67	5.65

an intensity of 100 mW/cm². In degrading the films we were careful to compensate for the partial transparency of the Pd contacts. Cell performance parameters were determined in both States A and B by Gautam Ganguly at BP Solar. The cell results determined by Gautam are for State A are summarized in Table III. For State B device efficiencies are roughly 1% lower than for State A. As had been determined for a previous series of BP Solar devices, there appears to be a clear inverse relation between the device performance and the growth rate.

The defect densities determined by DLCP for all four films is quite low, and appears reasonably uniform except at the largest profiling distances (within 1000Å of the substrate – see Fig. 7 for a representative set of profiles for one sample). However, this apparent increase in the profiles at large distance may actually be caused by the fact that the edge of the depletion region is running into the edge of the film at the substrate.

In Figure 8 we plot the DLCP defect densities obtained for all 4 samples in this series as a function of growth rate, both for State A and State B. In both states we see that the DLCP defect density does not vary in any clear way with growth rate (and hence neither with the device performance). This is consistent with our DLCP results for the previous set of BP Solar samples discussed in Section 4.1.

FIG. 7. Drive-level capacitance profiles for sample L2129 (3Å/s) in the dark annealed state. The measurement frequency was 11Hz for all temperatures. The total deep defect density is estimated by doubling the (spatially averaged) DLCP density at 360K. This would result in an estimated deep defect density in this case of $3.5 \times 10^{15} \text{ cm}^{-3}$.

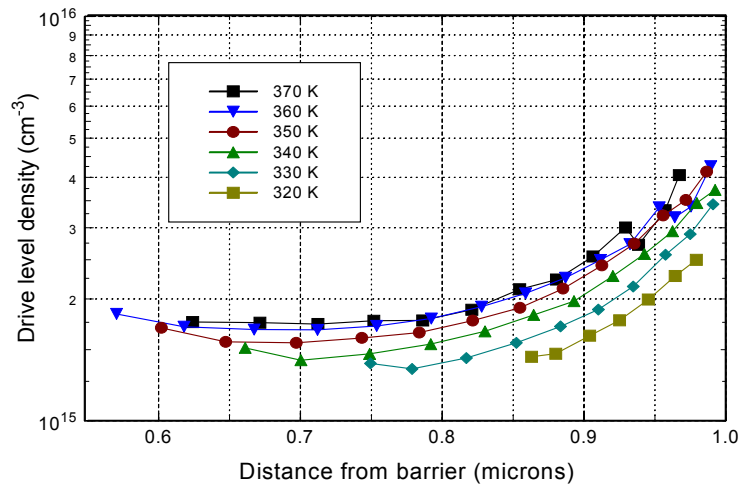
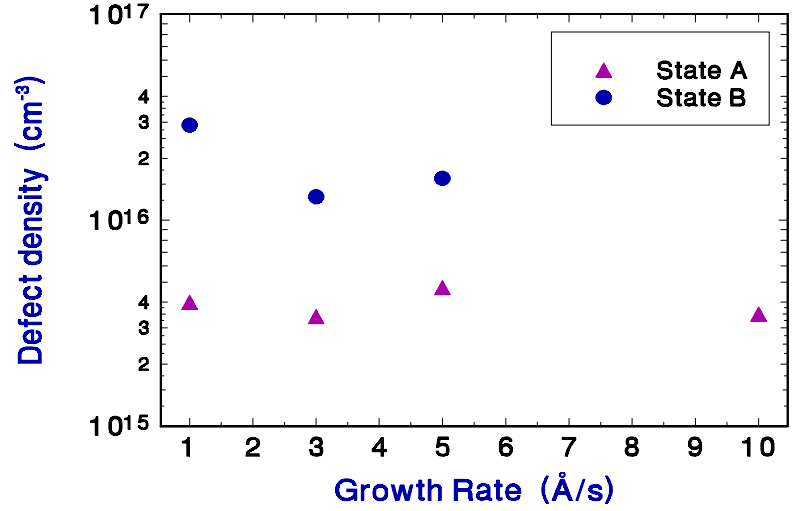


FIG. 8. Deep defect densities vs. growth rate for BP Solar films for both States A and B. These defect densities are estimated by *doubling* the 11Hz, 360K DLCP values. As with the results on a previous series of BP Solar samples, there appears to be little correlation between the deep defect density and the growth rate.



Next we determined the sub-band-gap spectra of these samples using transient photocapacitance spectroscopy. Two such spectra for the lowest growth rate sample (L2127) in State A are displayed in Fig. 9(a) (these two spectra were taken under different values of reverse bias to test for spatial dependence of the electronic properties). For this 1 Å/s growth rate sample

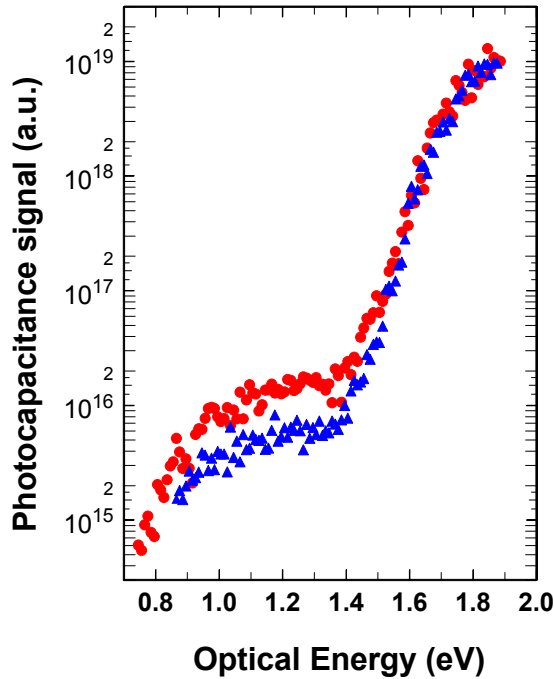


FIG. 9(a). Photocapacitance spectra for sample L2127 (1 Å/s) taken at 380K at two values of reverse bias: -3V (circles) and -1V (triangles). Thus these data indicate a higher defect density near the substrate interface.

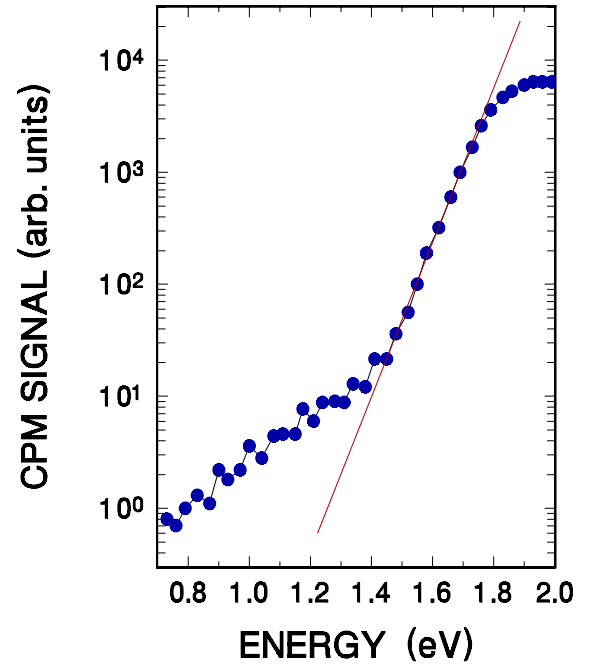


FIG. 9(b). CPM spectra obtained at NREL for the same sample. Note that the magnitude of the deep defect band is similar to the TPC spectra, but that the Urbach tail is much broader (61meV compared to less than 45meV for the TPC spectra).

the Urbach tail is quite narrow – it has a characteristic energy of less than 45 meV. Because these samples were also examined using CPM spectroscopy at NREL, it is quite interesting to compare the results of our photocapacitance measurements with the corresponding CPM spectra. In Fig. 9(b) the corresponding CPM spectrum for this sample is shown, also for State A. We observe that both spectra indicate a similar deep defect density; however, the shapes of the defect band clearly differ. Also, the Urbach energy deduced from the tail distributions is markedly different: it exceeds 60 meV for the CPM spectra. Such differences between these two types of sub-band-gap spectroscopy have been noted by us previously (for other sources of samples). It suggests to us that the CPM measurement reflects an additional broadening due to potential fluctuations over the transverse distance between the contacts. This could affect the secondary photocurrent signal which is the basis for the CPM measurements, but should not be an issue for the energy dependence of the transition rate that produces photocapacitance spectra.

For this series of 4 samples we found, in agreement with our results on the earlier BP Solar sample series, that the Urbach energies determined were correlated with growth rate such that higher growth rates exhibited broader band tails. The dependence of Urbach energy with growth rate is shown in Fig. 10. The matched device efficiencies are also indicated. In Table IV, we compare the void fractions determined by Don Williamson and the hydrogen content determined at NREL with the Urbach energies we have obtained from our TPC measurements. We note that, in all cases, a clear trend is apparent. We have also included the CPM determined Urbach

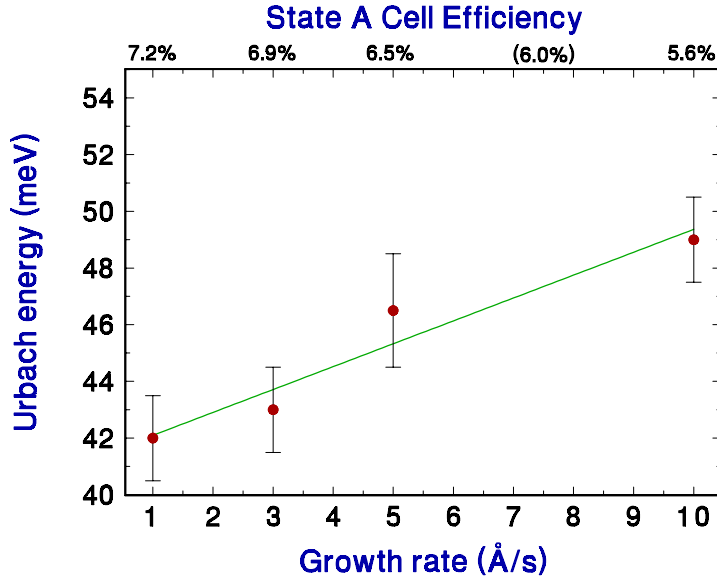


FIG. 10. Urbach energies determined from TPC spectra vs. film growth rate. These data suggest a reasonably strong correlation. Note also the matched device efficiencies for these growth rates indicated on the top scale.

TABLE IV. Comparison of TPC determined Urbach energies with growth rate, as well as hydrogen content (NREL), void fraction (CSM), and CPM determined Urbach energies (NREL).

Growth Rate (Å/second)	Hydrogen (at.%)	Void fraction (volume %)	TPC derived Urbach energy (meV)	CPM derived Urbach energy (meV)
1	10.4	0.02	42.0±1.5	60.7
3	11.6	0.08	43.0±1.5	57.4
5	12.2	0.08	46.5±2.0	62.6
10	16.1	0.6	49.0±1.5	---

energies in this Table. These do *not* exhibit a clear trend with growth rate. Indeed, the CPM determined Urbach energies are always significantly larger than those determined by TPC.

Finally, we have tried to gain some additional insight into the factors that may be responsible for the decrease in cell performance from our TPC spectra. Previously we had demonstrated that a comparison between transient photocapacitance (TPC) spectra and junction transient photocurrent (TPI) spectra were quite valuable because one could estimate the fraction of photo-excited holes that were able to escape the depletion region on the time scale of the transient measurement window. This estimate is based on the fact that the holes that escape will reduce the TPC signal magnitude while enhancing the TPI magnitude. Unfortunately, recording the companion TPI spectra is not possible on our current test devices that employ Schottky barrier junctions due to the presence of an internal photoemission signal that partially masks the junction photocurrent signal.

To overcome this problem we attempted an alternative approach; namely, we recorded the TPC spectra at two different temperatures. Examples of such pairs of photocapacitance spectra are shown in Fig. 11. The idea was to effectively prevent the holes from escaping the depletion region during the 200ms measurement time window by deep trapping them at a lower temperature, then repeating the measurement at a higher temperature such that they could now escape the traps within that time window. In the latter case, however, recombination would still limit the number of holes escaping. For our initial attempt with this method we employed the temperatures of 360K and 380K which, for a 0.9eV deep dangling bond defect, imply thermal detrapping times of roughly 0.4s and 0.09s, respectively.

The spectra in Fig. 11 show that, for the data on the 1Å/s sample, there is a clear reduction in the TPC signal in the bandtail region for the higher temperature. This indicates that a significant

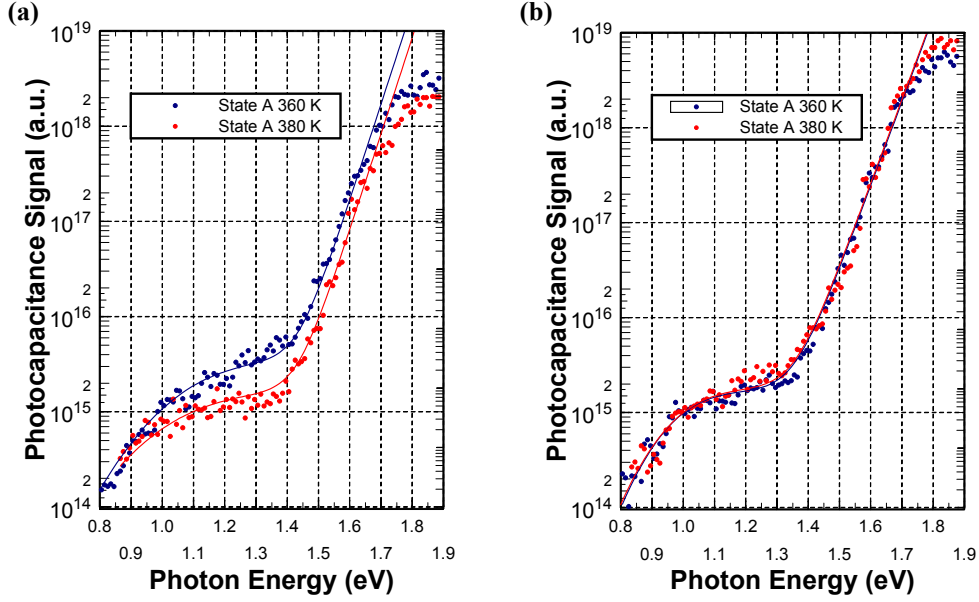


FIG. 11. Photocapacitance spectra for two BP Solar films in State A: **(a)** Sample L2127 deposited at $1\text{\AA}/\text{s}$, and **(b)** Sample 2137 deposited at $10\text{\AA}/\text{s}$. In each case the spectra have been recorded at two measurement temperatures: 360K and 380K. Note that there is a significant difference between the two spectra in (a), but not in (b).

fraction of holes (at least 65%) are able to escape the depletion region in 200ms at 380K. On the other hand, the spectra for the $10\text{\AA}/\text{s}$ sample appear identical at both temperatures. This indicates that very few holes are collected even at 380K. We believe this reduction of hole collection may be an important clue in identifying the predominant mechanism for the loss in device performance for the higher growth rate samples.

In retrospect the choice of 360K and 380K as temperatures to estimate the hole collection efficiencies may not be optimal. We have plans to take additional photocapacitance spectra over a larger range of temperatures to identify the best such temperatures to use for this purpose. In addition, we wish to check this approach using a-Si:H films deposited onto p^+ crystalline Si substrates so that TPI spectra may also be recorded. In this manner we hope to refine our approach so that we obtain the best possible estimates of the hole collection efficiencies for our “half device” test samples.

5.0 HOT-WIRE a-Si,Ge:H MATERIAL AT HIGH GERMANIUM FRACTION

In the past we examined a few a-Si,Ge:H alloy samples deposited by the hot-wire CVD method at NREL. We found quite good electronic properties for such material when the Ge fractions remained below 10at.%, but significantly poorer properties as this fraction exceeded

20at.%. Since our previous examination of such HWCVD a-Si_{1-x}Ge_xH alloys, considerable additional effort has been made at NREL toward improving these materials. During the past year we examined a couple additional samples deposited by HWCVD for films with much higher Ge levels. This was a collaboration initiated by Brent Nelson who sent us four a-Si_{1-x}Ge_xH films deposited on c-Si, quartz, and glass substrates. The details of the growth conditions have been described in Section 2.2.

Drive-level capacitance profiles for a 63at.% Ge sample (L753) are displayed in Fig. 12 for several measurement temperatures. These profiles indicate a deep defect density near 10^{16} cm^{-3} in the interior part of the film, but much larger and very non-uniform as we approach the top contact. This may reflect the general increase in substrate temperature during film growth (see

FIG. 12. Drive-level capacitance profiles at 33Hz for 63at.% Ge fraction a-Si_{1-x}Ge_xH film deposited by HWCVD at NREL. The very non-uniform density profiles may be a result of the variation in substrate temperature that occurred during growth.

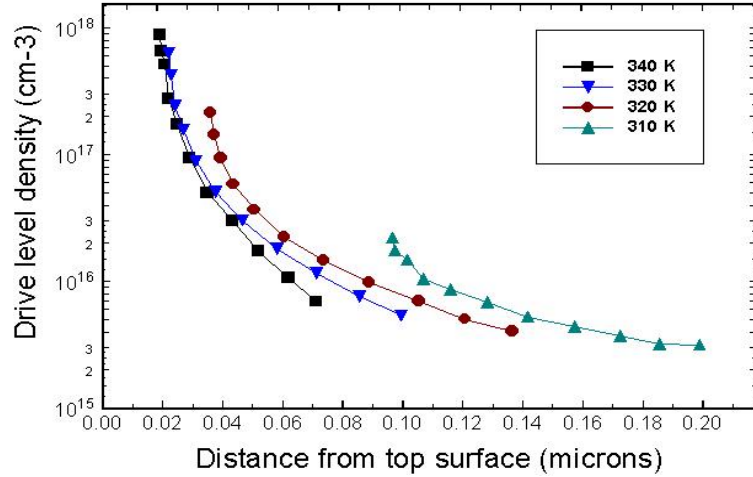


FIG. 13. Photocapacitance spectrum for the a-Si_{1-x}Ge_xH sample L753. The slope of the line, indicating the Urbach energy, is 70 meV. Also note the appearance of a defect band at energies below 1eV.

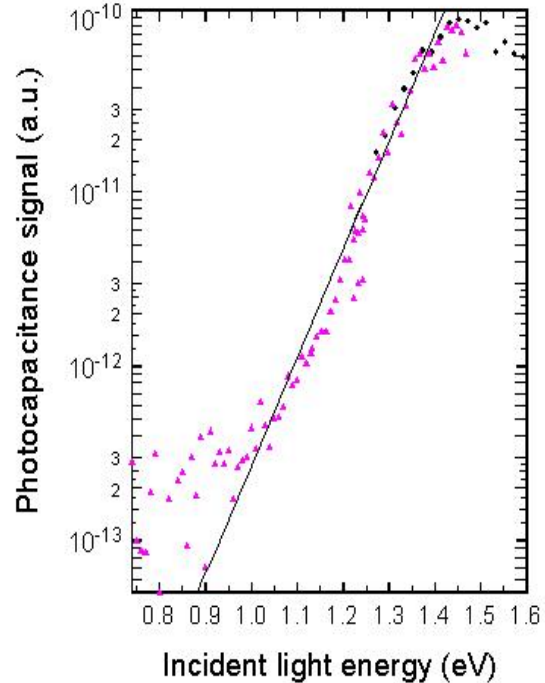


Table II). In Fig. 13 we display one of the photocapacitance spectra taken for this sample. This spectra indicates a rather broad bandtail (Urbach energy near 70meV) and an optical (E_{04}) gap close to 1.4eV. A deep defect band, consistent with a defect density in the mid 10^{16} cm^{-3} range is also exhibited below about 1.0 eV.

Although the results on this new series of HWCVD a-Si,Ge:H samples are somewhat limited, they do tend to agree with our earlier measurements of HWCVD alloy films indicating significantly broader bandtail slopes than for the best glow discharge a-Si,Ge:H alloy samples. Additional a-Si,Ge:H samples for us to study are now being scheduled for deposition at NREL. Hopefully, we will thus be able to assess the electronic properties of such HWCVD alloy material with Ge fractions exceeding 30at.% in the near future.

6.0 UNITED SOLAR AMORPHOUS SILICON NEAR PHASE BOUNDARY

As described in Section 2.3, during the current Subcontract year we obtained a couple of samples from United Solar Systems to explore the variation of properties above and below the transition to microcrystalline growth. These samples are largely amorphous in the central regime but, as one moves radially outward, become more amorphous (see Fig. 1). Thus, using one such sample film one can, in principle, explore properties ranging from nearly pure amorphous, through a mixed phase regime, to almost purely microcrystalline.

For our studies we deposited an array of 1mm diameter Pd dots over the film surface. Unfortunately, however, to date these types of contacts have resulted in robust Schottky barrier devices only for the portion of the film that was nearly in its purely amorphous phase. Thus, we have not yet been able to study the properties of this sample through its transition as we had hoped. On the other hand, we did manage to characterize the properties of the most amorphous portion in both its dark annealed (state A) and light degraded state (state B). A series of drive-level profiles we obtained for each of these metastable states for one particular Schottky device are displayed in Fig. 14.

In State A we found a defect density almost too small to measure in this $2\mu\text{m}$ thick film. That is, the increasing defect density beyond the $1.8\mu\text{m}$ position is almost certainly due to the fact that the edge of the depletion region is running into the n+ layer at the substrate. Thus, a rough estimate of the defect density would come from doubling the value of the 360K, 33Hz profile near $1.75\mu\text{m}$ where the profile begins to flatten. This gives $1.0 \times 10^{15} \text{ cm}^{-3}$.

After light soaking the depletion region becomes significantly smaller and this allows much more accurate profiles and densities to be probed. In this case we double the 350K, 11Hz to estimate the total deep defect density. A very low degraded value of $6 \times 10^{15} \text{ cm}^{-3}$ is obtained, and the sample properties appear to be quite spatially uniform.

FIG. 14(a). Drive-level profiles for a region near the center of film L13698 in its dark annealed state. We believe that the best estimate of the deep defect density is obtained from doubling the value of the 360K profile near $1.75\mu\text{m}$.

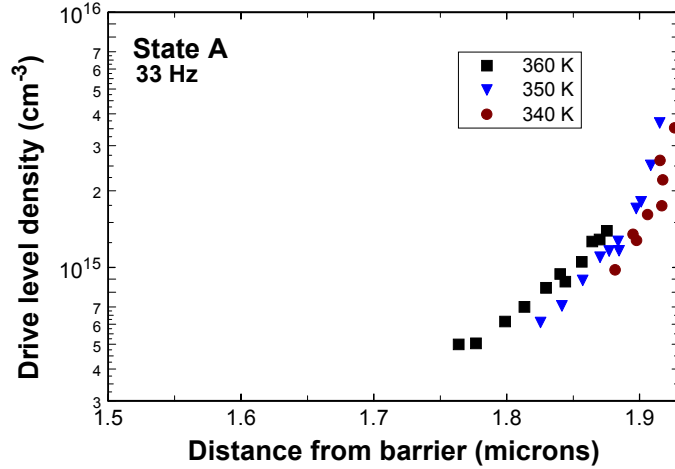
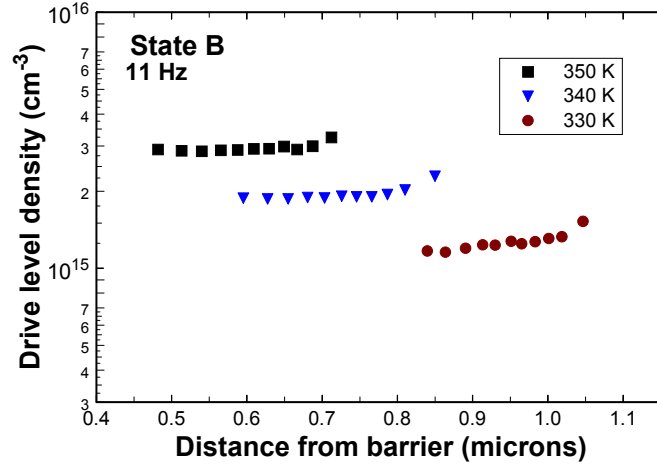


FIG. 14(b). Drive-level profiles for the same region of film L13698 after degrading by light soaking it for 100 hours at an intensity of $1\text{W}/\text{cm}^2$ (using a red filtered ELH light source). In this case very uniform profiles are obtained. We estimate a deep defect density of $6 \times 10^{15} \text{ cm}^{-3}$.



7.0 SUMMARY AND CONCLUSIONS

During this first phase of our NREL Subcontract period we have focused primarily upon our ongoing studies to try to identify the fundamental reasons that higher growth rate a-Si:H materials lead to devices with general lower performance. These studies utilized series of samples produced by Gautam Ganguly at BP Solar. The current work was motivated by our results in the previous year. There our measurements had revealed that the deep defect density determined by drive-level capacitance profiling (DLCP) did not change as the growth rate was varied; however, the Urbach energies deduced by transient photocapacitance (TPC) sub-band-gap spectroscopy *were* correlated with growth rate and hence also the device performance. In the past year we determined that the magnitude of the deep defect revealed in the TPC spectra actually correlated quite well with the device fill factors, even though the DLCP determined defect densities did not. This led us to propose that the capture cross section of the deep defects

were enhanced at the higher growth rates even though their actual density did not vary substantially.

This led into a second study in collaboration with BP Solar employing a new series of their samples. Our own measurements were actually only one part of a 5-way collaboration designed to obtain one the most complete set of data ever undertaken to compare device and material properties as a function of deposition rate. Results for this new series of samples agreed with the previous set in that the DLCP determined defect densities appeared to be largely uncorrelated with device performance, while the Urbach energies were strongly correlated. The other collaborative studies revealed that the void fraction and the hydrogen content were also quite strongly correlated with growth rate. (The cell performance once again exhibited a systematic decline in performance with increasing growth rate.)

At this point in time we can hypothesize that either the increased band-tail width (leading to a decreased effective hole mobility) or possibly the increase of deep defects with larger capture cross sections might be responsible. Either of these could be linked to the increased void fraction or changes in hydrogen microstructure. Additional studies will hopefully help resolve which of these is the more likely explanation.

During this past year we also examined a couple NREL HWCVD a-Si_{1-x}Ge_x:H alloy samples with Ge fractions exceeding 60at.%. These samples had somewhat poor electronic properties (non-uniform and somewhat high defect densities, very broad Urbach energies) in agreement with HWCVD a-Si_{1-x}Ge_x:H samples with higher Ge content we had measured previously. However, the devices being produced at NREL using their HWCVD alloys have been improving and we are looking forward to characterizing some of this more recently developed material in the near future.

Finally, we began a collaborative study with United Solar to examine material at or beyond the phase transition boundary to microcrystallinity. To date we have not been able to characterize samples that have any significant degree of microcrystalline component, but have plans to examine some p-i-n United Solar microcrystalline devices and some devices with an a-Si:H buffer layer on the top surface to enable us to create a good Pd Schottky barrier test device. We are also planning to look for a microcrystalline component in the low microcrystalline fraction material using our sub-band-gap TPC measurements.

Clearly, the characterization of micro- or nano-crystalline silicon materials (nc-Si:H) will become more of a focus of our efforts during the upcoming year. These materials seem to be quite promising as a substitute for the higher fraction a-Si_{1-x}Ge_x:H alloys for the narrow gap component of multijunction devices.

8.0 SUBCONTRACT SUPPORTED PUBLICATIONS

1. J. David Cohen, Jennifer Heath, Kimon C. Palinginis, Jeffrey C. Yang, and Subhendu Guha, "Insights into the mechanisms of light-induced degradation from studies of defects in low Ge fraction a-Si_{1-x}Ge_x:H alloys", J. Non-Cryst. Solids **299-302**, 449 (2002).
2. B. D. Chapman, S. -W. Han, G. T. Seidler, E. A. Stern, J. David Cohen, S. Guha and J. Yang, "Short-range compositional randomness of hydrogenated amorphous silicon-germanium films", J. of Appl. Phys. **92**, 801 (2002).
3. J. David Cohen, "Light-induced defects in hydrogenated amorphous silicon germanium alloys", Sol. Energy Mat. and Solar Cells, in press.
4. Jennifer Heath, James J. Gutierrez, J. David Cohen, and Gautam Ganguly, "Effect of increasing growth rates on film properties and device performance for the DC glow discharge amorphous silicon", Mat. Res. Soc. Symp. Proc. **715**, 553 (2002).

9.0 REFERENCES

1. J. Heath, S.B. Iyer, Y. Lubianiker, J.D. Cohen, and G. Ganguly, Mat. Res. Soc. Symp. Proc. **664**, A25.3 (2001)
2. J. Yang, K. Lord, B. Yan, A. Banerjee, and S. Guha, Mat. Res. Soc. Symp. Proc. **715**, 601 (2002).
3. D.V. Lang, J.D.Cohen, and J.P. Harbison, Phys. Rev. **B25**, 5285 (1982).
4. C.E. Michelson, A.V. Gelatos, and J.D. Cohen, Appl. Phys. Lett. **47**, 412 (1985).
5. K.K. Mahavadi, K. Zellama, J.D. Cohen, and J.P. Harbison, Phys. Rev. **B35**, 7776 (1987).
6. See, for example, T. Unold, J. Hautala, and J.D. Cohen, Phys. Rev. **B50**, 16985 (1994).
7. Lang, D.V. in *Thermally Stimulated Relaxation in Solids*, vol. 37 of Topics in Applied Physics, ed by P. Braunlich (Springer, Berlin, 1979), p. 93.
8. Cohen, J.D., in *Hydrogenated Amorphous Silicon*, vol. 21C of *Semiconductors and Semimetals*, ed. by J. Pankove (Academic Press, New York, 1984), p. 9.
9. J.D. Cohen and A.V. Gelatos, in *Advances in Disordered Semiconductors Vol I: Amorphous Silicon and Related Materials*, ed. by H. Fritzsche (World Scientific, Singapore, 1988), pp. 475-512.
10. J. David Cohen, Thomas Unold, A.V. Gelatos, and C.M. Fortmann, J. Non-Cryst. Solids **141**, 142 (1992).
11. T. Unold, J.D. Cohen, and C.M. Fortmann, Mat. Res. Soc. Symp. Proc. **258**, 499 (1992).
12. A.V. Gelatos, K.K. Mahavadi, and J.D. Cohen, Appl. Phys. Lett. **53**, 403 (1988).
13. X. Xu, J. Yang, S. and S. Guha, Appl. Phys. Lett. **62**, 1399 (1993).
14. B. von Roedern, Appl. Phys. Lett. **62**, 1368 (1993).
15. C.R. Wronski, J.M. Pearce, R.J. Koval, X. Niu, A.S. Ferlauto, J. Koh, and R.W. Collins, Mat. Res. Soc. Symp. Proc. **715**, 459 (2002).
16. See, for example, M. Gunes and C.R. Wronski, J. Appl. Phys. **81**, 3526 (1997).